Tomographic inversion of satellite photometry

Stanley C. Solomon, P. B. Hays, and Vincent J. Abreu

An inversion algorithm capable of reconstructing the volume emission rate of thermospheric airglow features from satellite photometry has been developed. The accuracy and resolution of this technique are investigated using simulated data, and the inversions of several sets of observations taken by the Visible Airglow Experiment are presented.

I. Introduction

Photometric measurements of atmospheric airglow from orbit yield the surface brightness of the emission in a given direction and over a finite field of view. To recover a spatially varying volume emission rate, an inversion algorithm must be applied to the data. The Visible Airglow Experiment[1] (VAE), a photometer and filter wheel instrument flown on the three Atmosphere Explorer spacecraft, yielded large amounts of highly resolved airglow data which have been subjected to several such inversions. While these algorithms have been successful in finding the emission function associated with many geophysical phenomena, we seek inversions with greater resolution and generality; in particular, the analysis of auroral and twilight emissions requires improved techniques because of their high spatial variability.

If an instrument's field of view is narrow, such as the ¾° half-cone of VAE channel 1, it may be approximated as a line. The emission function is then sampled by taking many of its line integrals, and the task of the inversion is to transform this function of line integrals back into the emission function. This problem is common to many remote sensing applications, including the well-known medical diagnostic procedure of computerized tomography. However, the airglow inversion problem is complicated by the lower atmosphere and solid earth which contaminate the airglow observations with scattered light and also block the instrument's view of all but a small segment of the emission function. Therefore, many techniques use only limb scan data—those measurements whose line of sight intersects the upper atmosphere but not the lower atmosphere or solid ground (Fig. 1). This is but a fraction of the VAE data, since the photometer was mounted so that it swept a full circle in the orbital plane once every 15 sec when the satellite was in a spinning mode.

The first inversion implemented on VAE data was the Abel inversion,[2] where it is assumed that the emission observed does not vary along the satellite track but only with altitude. This condition need not be strictly satisfied so long as there are no significant horizontal gradients within the portion of the emission intersected by the photometer's field of view at any given location. The Abel inversion is useful for a broad class of phenomenon but not for many regions of interest. Therefore, a 2-D algebraic reconstruction technique (ART) was employed.[3–5] In this procedure the atmosphere is segmented into an array of pixels, and each instrumental observation is considered to be the sum of emissions from each pixel which its line of sight intersects. The algorithm then solves the resulting system of linear equations using iterative relaxation. A similar analysis has been successfully applied to data from the horizon scanning photometer on OGO-6.[6,7] With VAE data, this technique may incorporate lines that intersect the earth provided scattered light from below can be calculated. But experimental data produce inconsistent systems of equations, which will not necessarily converge to a unique solution. Another inversion was subsequently developed for the purpose of analyzing features of moderate spatial variability in the equatorial region.[8] Limb scan data were used to recover 2-D volume emission rates using a modified algebraic procedure: The volume emission rate of the layer immediately under the satellite was calculated, that information was used to calculate the emission in the next lower layer, and so on to the lowest altitude observable. This results in a unique solution to the system of equations. However, any error in determining the emission at the top levels can propagate downward, producing fictitious oscillations in the alti-

The authors are with University of Michigan, Department of Atmospheric & Oceanic Science, Space Physics Research Laboratory, Ann Arbor, Michigan 48109.

Received 23 February 1984.
0003-6935/84/193409-06$02.00/0.

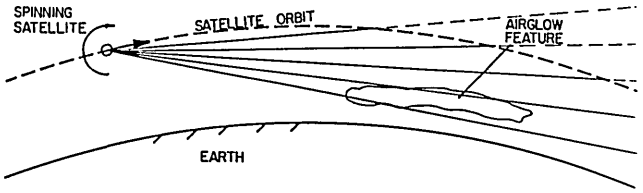

Fig. 1. Limb scans taken by a spinning satellite. Every fourth line of sight of VAE channel 1 is shown.

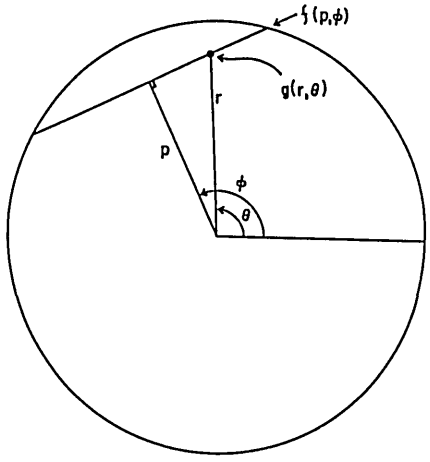

Fig. 2. Geometry of the Cormack inversion. Every line integral f is the sum of all $g(r,\theta)$ along a path specified by distance p and angle ϕ.

tude profiles. To prevent this the volume emission rate must be smoothed at each level, causing loss of resolution.

We have now developed a new inversion technique based on the work of Cormack in the early 1960s.[9,10] Cormack's solution must be implemented using only limb scan data, as shown below, and so may be applied to the VAE instrument without having to deal with the problem of scattered light from the earth. We have developed a procedure for the numerical integration of the Cormack inversion integral and tested the inversion on simulated data to study its behavior. We then inverted several segments of VAE data at various wavelengths. Some of these are presented as examples of the capabilities of this algorithm.

II. Theoretical Development

If the field of view of the instrument is sufficiently narrow, its measurements may be considered line integrals of the function which it observes. If absorption and time dependence can also be neglected, the problem reduces to the purely mathematical one of recovering a function which is specified by its line integrals. A function g of two polar variables (r,θ) may be expanded in a Fourier series with respect to the angular variable θ. A line integral through the domain of $g(r,\theta)$ may be uniquely specified by its perpendicular distance from the origin p and the angle ϕ, which that perpendicular makes with some reference direction (Fig. 2). The line integrals are then also a function $f(p,\phi)$, which may also be expanded in a Fourier series with respect to ϕ. Cormack then derived[9]

$$G_n(r) = \frac{-1}{\pi}\frac{d}{dr}\int_r^\infty \frac{rF_n(p)T_n(p/r)dp}{p(p^2-r^2)^{1/2}}, \tag{1}$$

where $G_n(r)$ is the nth Fourier coefficient of $g(r,\theta)$, $F_n(\mathrm{p})$ is the nth Fourier coefficient of $f(p,\phi)$, and T_n is the nth Chebyshev polynomial. This equation in principle allows one to obtain $g(r,\theta)$ from knowledge of its line integrals.

The equation may be modified by differentiating under the integral and integrating by parts to obtain

$$G_n(r) = \frac{-1}{\pi}\int_r^\infty \frac{\frac{d}{dp}F_n(p)T_n(p/r)dp}{(p^2-r^2)^{1/2}}. \tag{2}$$

In this form, the relationship of the Cormack inversion to the Abel inversion may be better understood. The Abel inversion

$$g(r) = \frac{-1}{\pi}\int_r^\infty \frac{\frac{d}{dp}f(p)dp}{(p^2-r^2)^{1/2}} \tag{3}$$

is equivalent to the zeroth Fourier term of the Cormack inversion since $T_0(p/r) = 1$. This is not surprising since the zeroth Fourier term has no angular variation—the crucial assumption behind the Abel inversion. The Cormack inversion also shares with the Abel inversion the property that the recovered function at radius r depends only on values of line integrals with $p > r$, as can be seen from inspection of Eq. (1) or (2). Thus it is an appropriate inversion for limb scan observations but not for observations looking down at the solid earth.

The evaluation of the integral in Eq. (2) introduces some difficulties because of the singularity at $p = r$. We solved this problem by fitting parabolic splines to the $F_n(p)$. To perform the integration between two levels r_1 and r_2, the $F_n(p)$ are fitted by $Ap^2 + Bp + C$, the change of variable $x = p/r$ is made, and the equation becomes

$$-\pi G_n(r) = 2A_r\int_{r_1}^{r_2}\frac{xT_n(x)dx}{(x^2-1)^{1/2}} + B\int_{r_1}^{r_2}\frac{T_n(x)dx}{(x^2-1)^{1/2}}. \tag{4}$$

Let

$$I_{m,n} = \int_{r_1}^{r_2}\frac{x^m T_n(x)dx}{(x^2-1)^{1/2}}. \tag{5}$$

Using the Chebyshev recursion relation, we derive $I_{m,n} = 2I_{m+1,n} - I_{m,n-2}$. Since $T_0(x) = 1$ and $T_1(x) = x$: the $I_{m,1} = I_{m+1,0}$. So if the $I_{m,0}$ can be found, the $I_{m,n}$ may be calculated recursively. Fortunately,[11]

$$I_{m,0} = \frac{x^{m-1}(x^2-1)^{1/2}}{m} + \frac{m-1}{m}I_{m-2,0} \tag{6}$$

$I_{0,0}$ and $I_{1,0}$ are known, so the $I_{m,n}$ may then be evaluated. This is done for each slab from r to infinity (generally the satellite altitude) and the results summed to obtain the $G_n(r)$. Rather than evaluating these integrals from scratch for each inversion, the coefficients of each term of the $I_{m,n}$ have been precalculated for $m = 0,1$ and $n = 1,2,\ldots,n_{\max}$, where $n_{\max}$ is the number

of Fourier coefficients to be retained in the inversion. A comparatively efficient algorithm results.

III. Implementation and Simulation

Many airglow emissions are optically thin and vary slowly with time. The time variation may be neglected if it is of a scale >200 sec, which is the approximate time from when the instrument first sees a feature on the horizon until the satellite passes over it. If the instrumental field of view is narrow enough so that column brightness measurements of an optically thin, slowly changing feature may be considered to occur along a single ray instead of a cone, the procedure described above may be used to recover a 2-D slice of the volume emission rate.

Emission features were simulated and sampled at the VAE data rate using numerical integration along the lines of sight. The 32-msec integration period of channel 1 translates to ~¾° of spin angle per count, and the satellite moves along its track ~1° (or 110 km)/spin. The simulated data were then subjected to the inversion procedure to evaluate its efficacy. Figure 3 presents the results from an idealized case where noise and field of view broadening are not included. In Fig. 3(a), imaginary auroral emissions are displayed. The emissions were generated by multiplying Chapman functions in height by Gaussians in angle along track. The feature on the left used a Chapman function based on a scale height of 30 km and a Gaussian of halfwidth of 2.9°; the one on the right employed a 15-km scale height and a 4.0° halfwidth. The simulated data were interpolated onto an annular grid in p,ϕ space using bivariate linear interpolation. The archlike shapes in Fig. 3(b) are typical observation patterns of discrete features. The Fourier series was truncated after 40 terms as this was the point where roundoff error in the recursive calculation of the integration coefficients became a problem, and because at values of >40, interpolation truncation error began to dominate the algorithm. The inversion reproduces the form of the feature fairly well [Fig. 3(c)] and recovers the total emission rate within 1%, but the features are smeared horizontally and the vertical profile is also slightly flattened. These effects are due to truncation of the Fourier series and, in the case of the vertical profile, to the limited instrumental resolution with respect to tangent height p.

This last effect is magnified by the photometer's field of view, as can be seen in Fig. 4. Here Gaussian noise with a halfwidth equal to the square root of the number of counts has also been added. A sensitivity of 10 R/count was assumed typical of VAE channel 1. The field of view broadening effect has been included in this simulation by integrating over a cone instead of a line. The motion of the photometer during its counting period is incorporated into the field of view integration so that an effective half-cone of ~1.2° is employed.

Noise in the data introduces spurious high frequencies into the recovered volume emission rate, which must be filtered out by appropriate truncation of the Fourier spectrum. Because the inversion of the lowest levels depends on the accurate measurement of the

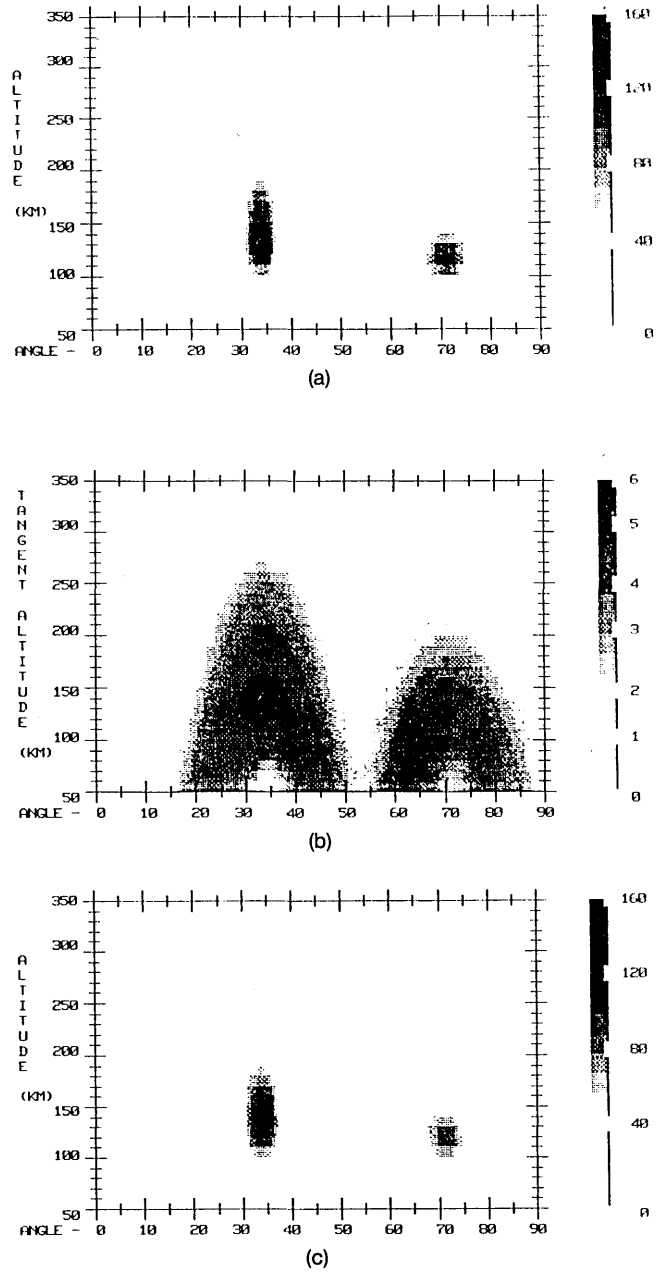

Fig. 3. (a) Imaginary airglow feature. Units are arbitrary but may be thought of as tens of photons cm^{-3} sec^{-1}. (b) Column brightness observed by the instrument as a function of p and ϕ. Units are arbitrary but may be thought of as $\log_{10}$ rayleighs. (c) Estimate recovered by the inversion.

levels above them, the spurious values start at lower frequency at low altitudes than at higher ones and are thus recognizable by their slanted profile. The contamination was removed by applying a Gaussian-shaped filter to tail off the offending terms, retaining progressively more terms at higher altitudes to correspond to the characteristic shape of the erroneous values. For this simulation, 30 terms were retained at the bottom (50 km), and one term was added every 20 km until at 250 km and above all 40 terms were used.

Noise and field of view broadening degrade the quality of the inversion by further smearing in both the

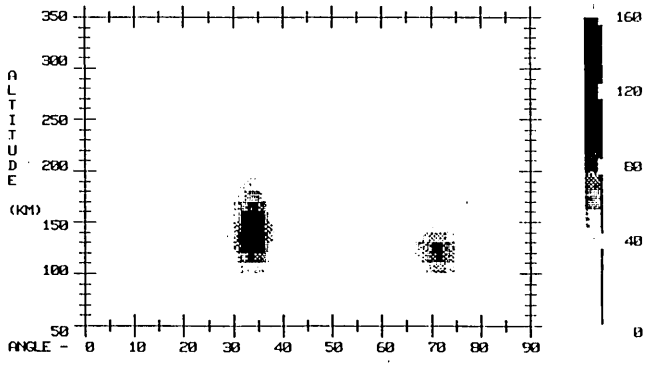

Fig. 4. Estimate recovered when noise and field of view broadening were added to the simulation.

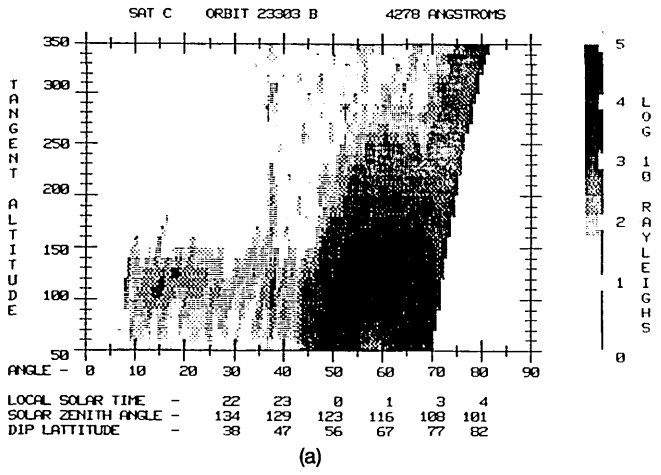

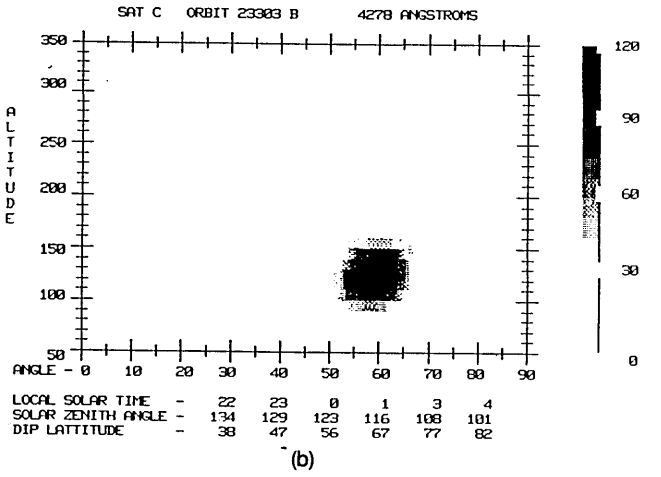

Fig. 5. 4278-Å emission from the $1NG$ band system of N_2^+. (a) The interpolated data are plotted logarithmically. (b) The estimated volume emission rate from the Cormack inversion is plotted linearly.

horizontal and vertical directions, but in this case the total recovered emission rate is still within 1% of the original. The presence of noise reduces the number of Fourier terms that may be used in the inversion, thus the estimated peak emission of a discrete feature is reduced, which flattens the recovered altitude profile. The instrument's field of view and integration period decrease the accuracy of the limb scan, which also reduces the estimated peak emission and broadens the altitude profile. Thus noise is a problem for emissions which have sharp horizontal variations while the integration period and field of view are a problem for thin emission layers. For example, the inversion of the simulated feature on the left in Fig. 3(a) is reduced at its peak to 77% of the original when the VAE channel 1 data rate is simulated, to 67% when noise is added, and to 60% when the field of view is simulated, both with and without noise. However, for a very broad feature based on the same Chapman function, the reductions are to 93, 92, and 85%, respectively. Thus, it may be seen that the errors engendered by this inversion depend not only on the instrumental parameters but also on the emission function.

IV. Inversion of VAE Data

The algorithm was then applied to several orbits from the VAE data base. The background emission external to the satellite's orbit was subtracted using a procedure similar to that employed in the 2-D inversion of Fesen and Hays.[8] Forward-looking scans and backward-looking scans were inverted separately to minimize the effects of any time-dependent phenomena. Since the photometers were often turned on or off in the midst of the dayglow or the auroral oval, each data set had to be truncated, preferably at a local minimum, and the edges faired down to zero. The unobserved parts of the orbit were also set equal to zero.

The $G_n(r)$ were bandlimited, as in simulation, but we were unable to retain as many terms as in the simulated case without badly oscillating results. Experimental error, temporal changes in the emission function, the finite instrumental field of view, and interpolation truncation error interact to produce spurious values for the $G_n(r)$, starting at the lowest levels for n approximately 20, then working up to higher altitudes for higher values of n. These terms were filtered out using the technique described above but with only 20 to 25 terms retained at the lowest altitude. Naturally, this places a limit on how sharp a feature may be reconstructed.

Figure 5 presents results from the 4278-Å filter, which measures emission from N_2^+ in the $1NG$ band system. This emission is caused in the aurora by electron impact excitation and follows the total ionization rate profile.[12] The orbit is an oblique cut through the nightside auroral oval near Fairbanks, Alas. and has been previously studied by a combination of ground- and satellite-based instruments.[13,14] The inversion shows the emission to be confined to a narrow altitude band near 120 km, as expected. An altitude profile taken from the middle of the feature is shown in Fig. 6. The profile recovered by the inversion is somewhat broader than the actual altitude dependence due to instrumental smearing of the limb scan data. When this profile is integrated with respect to height, a column brightness of 750 R is calculated. This value is only ~40% of the column brightness observed from orbit while the satellite was

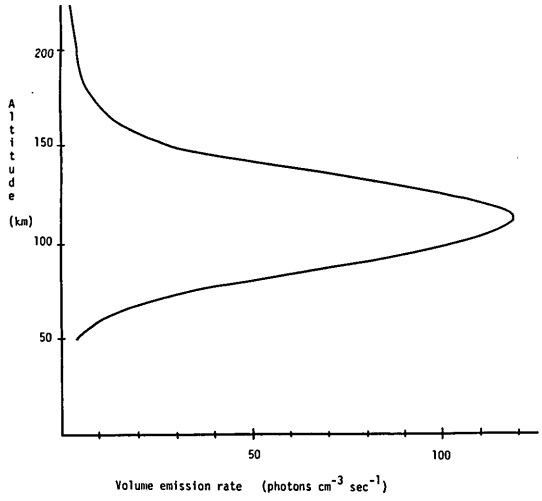

Fig. 6. Altitude profile taken through the peak of the aurora seen in Fig. 5.

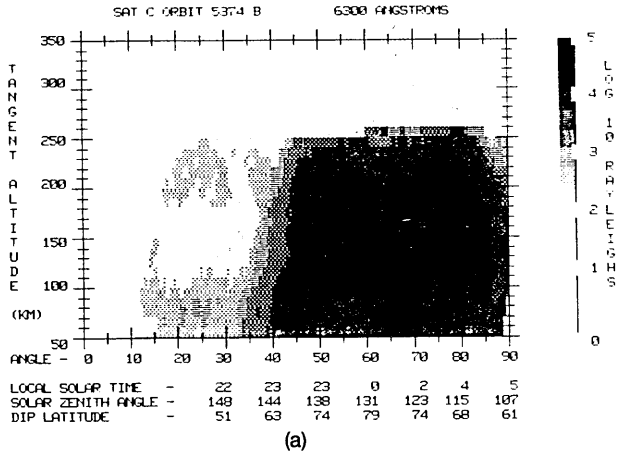

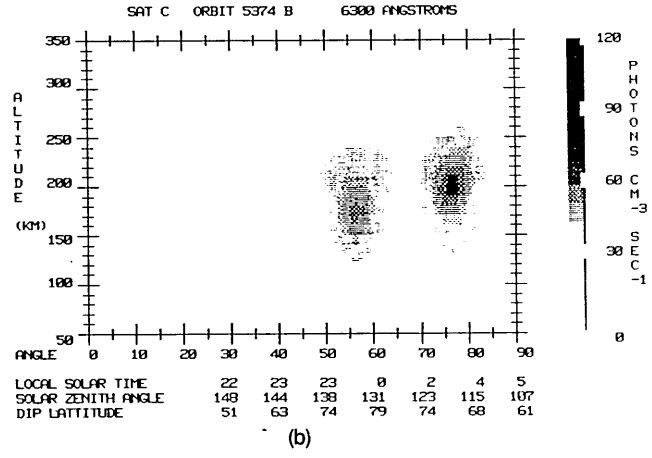

Fig. 7. 6300-Å emission of atomic oxygen arising from the ($3P$–$1D$) transition.

directly above (with the estimated ground brightness subtracted), but away from the peak the inversion estimate is greater than the column brightness measurements.[14] This effect is due to the characteristic horizontal smearing observed in simulation and is caused

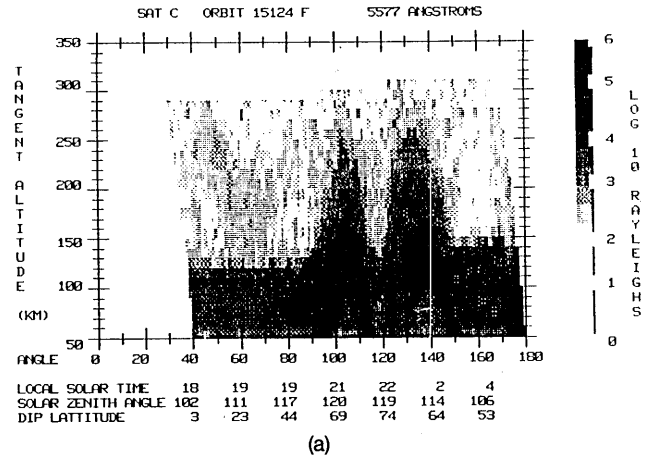

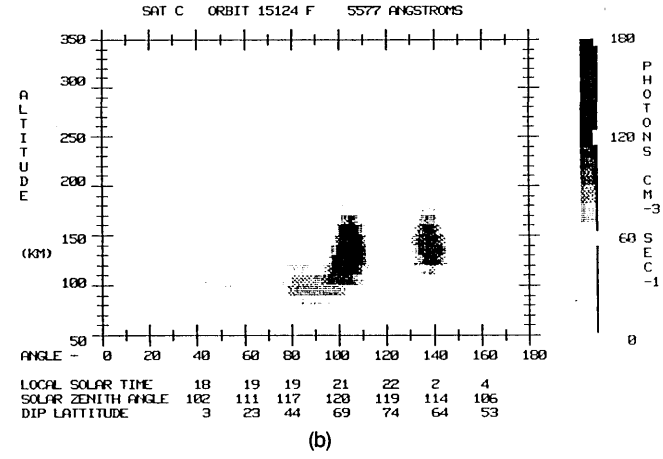

Fig. 8. 5577-Å emission from the ($1D$–$1S$) transition of atomic oxygen. The dayglow seen coming in from the right in (a) was excluded in performing the inversion displayed in (b).

by the combined effect of field of view broadening and filtering of the high frequencies. When the recovered volume emission rate function is integrated over the r,θ plane, a total emission is found which matches the column brightnesses integrated along the satellite track within 10%.

The 6300-Å auroral emission from the ($3P$–$1D$) transition of atomic oxygen is shown in Fig. 7 to extend above 200 km in contrast to the lower 4278-Å feature. The satellite passes over the aurora in the premidnight sector and then again in the predawn sector as it heads equatorward. In this case, the altitude of the aurora is markedly higher in the predawn sector.

Figure 8 shows the 5577-Å emission of atomic oxygen resulting from the ($1D$–$1S$) transition. This figure is particularly interesting because the data set is sufficiently large that we may observe the twilight/nighttime layer at ~100 km, followed by a cut through the auroral oval, darkness over the polar cap, and then another cut through the aurora. The inversion indicates that the 100-km layer disappears underneath the aurora, but this is probably another artifact of the field of view problem—the instrument is not capable of accurately resolving a faint layer under a bright feature. The field

of view also broadens the 100-km layer with respect to altitude—it is known to be much sharper than indicated in this inversion.

V. Discussion

All inversion algorithms operate on a finite set of measurements, whereas mathematical treatments may assume an infinite number of line integrals. Thus any result, no matter how precise the observations or how perfect the algorithm, yields but an estimate of the original function. By modeling the instrumental parameters and simulating typical airglow and auroral phenomena, it is possible to obtain some insight into the manner in which the estimated emission function differs from the actual. The Cormack inversion has the desirable quality of being an analytic, as opposed to iterative, technique. But high spatial frequencies must still be filtered out of the inverted data, as there will always be an upper limit to the instrument's ability to discriminate spatial variability. One advantage to this method is that by operating in Fourier space, such filtering becomes straightforward. This attribute is shared by several other algorithms which have been successful in other fields but are difficult to apply to airglow observations.

The implementation of this algorithm represents a significant step forward for the Visible Airglow Experiment, particularly with respect to obtaining the altitude variation of discrete features. We intend to employ it in future studies of auroral, twilight, and equatorial airglow. We also intend to develop a procedure for incorporating the downward-looking data from nocturnal orbits to sharpen the horizontal resolution of the recovered volume emission rate function.

This work was supported by NASA grant NAGW-496 to the University of Michigan.

References

1. P. B. Hays, G. Carignan, B. C. Kennedy, G. G. Shepherd, and J. C. G. Walker, "The Visible Airglow Experiment on Atmospheric Explorer," Radio Sci. **8**, 369 (1973).
2. R. G. Roble and P. B. Hays, "A Technique for Recovering the Vertical Number Density Profile of Atmospheric Gasses from Planetary Occultation Data," Planet. Space Sci. **20**, 1727 (1972)
3. R. Gordon, R. Bender, and G. T. Herman, "Algebraic Reconstruction Techniques (ART) and Three-Dimensional Electron Microscopy and X-ray Photography," J. Theoret. Biol. **29**, 471 (1970).
4. R. Gordon and G. T. Herman, "Three-Dimensional Reconstruction from Projections, a Review of Algorithms," Int. Rev. Cytol. **38**, 11 (1974).
5. P. B. Hays, D. W. Rusch, R. G. Roble, and J. C. G. Walker, "The OI (6300A) Airglow," Rev. Geophys. Space Phys. **16**, 225 (1978).
6. R. J. Thomas and T. M. Donahue, "Analysis of OGO-6 Observations of the OI 5577 Å Tropical Nightglow," J. Geophys. Res. **77**, 3557 (1972).
7. B. Wasser and T. M. Donahue, "Atomic Oxygen Between 80 and 120 km: Evidence for a Latitudinal Variation in Vertical Transport near the Mesopause," J. Geophys. Res. **84**, 1297 (1979).
8. C. G. Fesen and P. B. Hays, "Two-Dimensional Inversion Technique for Satellite Airglow Data," Appl. Opt. **21**, 3784 (1982).
9. A. M. Cormack, "Representation of a Function by its Line Integrals with Some Radiological Applications," J. Appl. Phys. **34**, 2722 (1963).
10. A. M. Cormack, "Representation of a Function by its Line Integrals, with some Radiological Applications, II," J. Appl. Phys. **35**, 2906 (1964).
11. I. Gradshteyn and I. Ryzhik, *Table of Integrals, Series, and Products* (Academic, 1983).
12. A. Vallance Jones, *Aurora* (Reidel, Hingham, Mass., 1974).
13. V. J. Abreu and P. B. Hays, "Parallax and Atmospheric Scattering Effects on the Inversion of Satellite Auroral Observations," Appl. Opt., **20**, 2203 (1981).
14. M. H. Rees and V. J. Abreu, "Auroral Photometry from the Atmosphere Explorer Satellite," J. Geophys. Res. **89**, 317 (1984).